Comprehensive spectroscopic and photometric study of pulsating eclipsing binary star AI Hya

F. Kahraman Aliçavuş [ORCID],[1,2]★ T. Pawar,[3] K. G. Hełminiak [ORCID],[3] G. Handler,[4] A. Moharana [ORCID],[3]
F. Aliçavuş [ORCID],[1,2] P. De Cat [ORCID],[5] F. Leone,[6,7] G. Catanzaro [ORCID],[7] M. Giarrusso,[7,8] N. Ukita[9,10] and E. Kambe[11]

[1]*Faculty of Science, Physics Department, Çanakkale Onsekiz Mart University, TR-17100 Canakkale, Turkey*
[2]*Astrophysics Research Center and Ulupınar Observatory, Çanakkale Onsekiz Mart University, TR-17100 Çanakkale, Turkey*
[3]*Department of Astrophysics, Nicolaus Copernicus Astronomical Center, ul. Rabiańska 8, PL-87-100 Toruń, Poland*
[4]*Nicolaus Copernicus Astronomical Center, Polish Academy of Sciences, Bartycka 18, PL-00-716 Warsaw, Poland*
[5]*Royal Observatory of Belgium, Ringlaan 3, B-1180 Brussel, Belgium*
[6]*Dipartimento di Fisica e Astronomia, Sezione Astrofisica, Università di Catania, Via S. Sofia 78, I-95123 Catania, Italy*
[7]*INAF, Osservatorio Astrofisico di Catania, Via S. Sofia 78, I-95123 Catania, Italy*
[8]*Department of Physics and Astronomy, University of Florence, Via Giovanni Sansone 1, I-50019 Sesto Fiorentino, Italy*
[9]*Okayama Astrophysical Observatory, National Astronomical Observatory of Japan, 3037-5 Honjo, Kamogata, Asakuchi, Okayama 719-0232, Japan*
[10]*The Graduate University for Advanced Studies, 2-21-1 Osawa, Mitaka, Tokyo 181-8588, Japan*
[11]*Subaru Telescope, National Astronomical Observatory of Japan, 650 North Aohoku Place, Hilo, HI 96720, USA*

ABSTRACT

The pulsating eclipsing binaries are remarkable systems that provide an opportunity to probe the stellar interior and to determine the fundamental stellar parameters precisely. Especially the detached eclipsing binary systems with (a) pulsating component(s) are significant objects to understand the nature of the oscillations since the binary effects in these systems are negligible. Recent studies based on space data have shown that the pulsation mechanisms of some oscillating stars are not completely understood. Hence, comprehensive studies of a number of pulsating stars within detached eclipsing binaries are important. In this study, we present a detailed analysis of the pulsating detached eclipsing binary system AI Hya which was studied by two independent groups with different methods. We carried out a spectroscopic survey to estimate the orbital parameters via radial velocity measurements and the atmospheric parameters of each binary component using the composite and/or disentangled spectra. We found that the more luminous component of the system is a massive, cool and chemically normal star while the hotter binary component is a slightly metal-rich object. The fundamental parameters of AI Hya were determined by the analysis of binary variations and subsequently used in the evolutionary modelling. Consequently, we obtained the age of the system as 850 ± 20 Myr and found that both binary components are situated in the δ Scuti instability strip. The frequency analysis revealed pulsation frequencies between 5.5 and $13.0\,\mathrm{d^{-1}}$ and we tried to estimate which binary component is the pulsating one. However, it turned out that those frequencies could originate from both binary components.

Key words: stars: atmospheres – binaries: eclipsing – stars: fundamental parameters – stars: individual: AI Hya – stars: variables: δ Scuti.

1 INTRODUCTION

To understand the Universe, it is necessary to comprehend stars which are its building blocks. For a deep investigation of stars, we should know their basic stellar parameters such as mass (M), radius (R), and chemical composition. Binary stars, in particular the eclipsing ones, are the most suitable objects to derive these parameters as M and R can be derived with an accuracy better than 1 per cent (Torres, Andersen & Giménez 2010; Southworth 2013). Therefore, these systems are substantial for a better understanding of the Universe, our Galaxy, and, most directly, stellar evolution. However, eclipsing binary systems as such do not provide information about the stellar

interior. This is where the pulsating stars come in. The oscillation frequencies of pulsating stars can be used to probe the stellar interior by applying asteroseismic methods, making eclipsing binary systems with (a) pulsating component(s) one of the most valuable tools to improve our knowledge of stellar evolution.

Various types of pulsating stars in different evolutionary states exist. Some of them, such as β Cephei, δ Scuti, and γ Doradus stars (Lampens 2021; Southworth 2021), are also found in eclipsing binary systems. The δ Scuti variables are the most common pulsating stars found in eclipsing binaries because of their relatively short pulsation periods. The δ Scuti stars are A- to F-type dwarf or giant stars generally exhibiting pressure mode oscillations with periods between 18 min and 8 h and amplitudes below $0^m.1$ in the V band (Aerts, Christensen-Dalsgaard & Kurtz 2010). Their theoretical instability strip (e.g. Dupret et al. 2005) indicates the location of objects in

★ E-mail: filizkahraman01@gmail.com, filizkahraman@comu.edu.tr

the Hertzsprung–Russell (H–R) diagram that are expected to show δ Scuti-type oscillations. Thanks to space missions such as *Kepler* (Borucki et al. 2010) and the Transiting Exoplanet Survey Satellite (*TESS*; Ricker et al. 2014), we learned that δ Scuti stars are also observed beyond the borders of the theoretical instability strip, showing the necessity to revise them (Uytterhoeven et al. 2011; Antoci et al. 2014; Bowman & Kurtz 2018). According to the latest catalogue of δ Scuti stars in eclipsing binaries, there are around 90 such objects (Kahraman Aliçavuş et al. 2017). This number is now increasing especially by the discoveries of new systems from the investigation of the space data (e.g. Gaulme & Guzik 2019; Kahraman Aliçavuş et al. 2022). The pulsations of the δ Scuti stars in eclipsing binaries are affected by the other binary component (Kahraman Aliçavuş et al. 2017; Liakos & Niarchos 2017). Indeed, their pulsation period (P_{puls}) decreases when the orbital period (P_{orb}) becomes shorter and, hence, the other component approaches the pulsating component. It was also thought that the tidal forces between the binary components can alter the pulsation axis (Kurtz et al. 2020). The first observational proof of this was presented by Handler et al. (2020) thanks to the high-quality data of *TESS*. These authors showed that in some binary systems the pulsation axis can align with the orbital axis because of the tidal forces. This type of object is now known as tidally tilted pulsators and they are a clear proof of binary effects on pulsations.

For a deep understanding of the effects of binarity on pulsations in eclipsing binary systems and on stellar evolution and structure, comprehensive investigations of such systems are necessary. AI Hya ($V = 9^m.35$) is an eclipsing binary system with a δ Scuti component consisting of a F2m and F0V star (Stancliffe et al. 2015). It has an eccentric orbit and an orbital period of 8.289649(2) d (Kreiner 2004). Spectroscopic observations revealed that AI Hya is a double-lined binary system (Popper 1988). In a recent study, an updated photometric analysis based on the *TESS* data of AI Hya was given which shows that the secondary component exhibits multiperiodic oscillations (Lee, Hong & Kristiansen 2020). However, no detailed spectral analysis with high-resolution spectra has been carried out for the system so far. Therefore, we provide a detailed photometric and spectral analysis of AI Hya in this study to reveal the true character of this interesting object.

Two teams were working on this system independently. One group was led by TP (group-P with KH, AM, NU, and EK) and the second group by FKA (group-K with GH, FA, PDC, FL, GC, and MG). We used the same photometric but different spectroscopic data. We compared our partial results as the work progressed. However, the overall approach used by each group was different. In the end, we combined our results to obtain the final parameters of the system. The paper is organized as follows. In Section 2, the observational data are introduced. The radial velocity and spectral analyses are given in Sections 3 and 4, respectively. The binary modelling and the pulsation frequency analysis are presented in Sections 5 and 6, respectively. In Section 7, discussions and conclusions are given.

2 OBSERVATIONAL DATA

In the photometric analysis of AI Hya, *TESS* data were used by both groups. *TESS* was launched in 2018 April mainly to detect new exoplanets (Ricker et al. 2014). *TESS* has monitored almost the entire sky which has been subdivided into sectors that are observed for about 27 d each. The *TESS* observations were taken in 2-min short (SC) and 30-min long (LC) cadence in the nominal phase of the mission (first two years). For the extended mission, the LC was reduced to 10 min. The data are available in the Barbara A. Mikulski Archive for

Table 1. Information about the spectroscopic observations. *N*, *R*, and SNR represent the number of the spectra, resolving power and the signal-to-noise ratio, respectively.

Spectrometer	N	Observations (yr)	R	SNR	Spectral range (Å)
CAOS	1	2021	38 000	50	415–670
CORALIE	3	2015	60 000	20–34	390–680
HERMES	15	2020	85 000	50–70	377–900
HIDES	13	2014–2017	50 000	40–88	408–752

Telescopes (MAST)[1] where they are released in different versions: simple aperture photometry (SAP) and pre-search data conditioning SAP fluxes (PDCSAP). AI Hya was observed in one sector only (sector 7). The 2-min SAP fluxes were used in our analysis since SAP fluxes have lower flux uncertainty and 2-min data are more suitable for the analysis of AI Hya (see Section 6). They were converted into magnitude by using the same method as Kahraman Aliçavuş et al. (2022).

Photometric data from ground-based surveys also exist, e.g. from ASAS 3 (Pojmański 2002) and ASAS-SN (Jayasinghe et al. 2018), but they are of inferior quality and do not allow for proper analysis of pulsations. The *TESS* sector 7 data are the best ones available so far, although AI Hya will again be visible in the satellite's field of view in sector 61.

The spectroscopic data of the system were taken from four different instruments. The list of the instruments and the basic information about them are given in Table 1. One spectrum was taken with *Catania Astrophysical Observatory Spectropolarimeter* (CAOS; Leone, et al. 2016). The CAOS is a high-resolution, fibre-fed, cross-dispersed Échelle spectrograph installed to the 91-cm telescope at the Catania Astrophysical Observatory (Mt. Etna, Italy). Three spectra of AI Hya were collected from the CORALIE Échelle spectrograph which is mounted on the 1.2-m Leonhard Euler telescope at La Silla Observatory (Chile) (Pepe et al. 2018). The *High Efficiency and Resolution Mercator Échelle spectrograph* (HERMES) was also used to obtain high-resolution spectra of AI Hya. HERMES is mounted on the 1.2-m Mercator telescope at the Roque de Los Muchchos observatory on the Canary Island La Palma in Spain (Raskin et al. 2011). The last instrument used in this study is the *HIgh-Dispersion Échelle spectrograph* (HIDES). HIDES is attached to the 1.88-m telescope of Okayama astrophysical observatory in Japan (Kambe et al. 2013). The spectra of CORALIE and HIDES were taken by group-P, while the spectra of CAOS and HERMES were gathered by group-K. In total 32 spectra of AI Hya were gathered and these spectra are well distributed in orbital phases of AI Hya. Each group used the obtained spectra to measure the radial velocity (v_r) changes. Additionally, these data were taken into account to derive the atmospheric parameters (e.g. effective temperature T_{eff}, surface gravity log g, metallicity) and the projected rotational velocity ($v \sin i$) of the components of AI Hya.

3 RADIAL VELOCITY ANALYSIS

The v_r values of the AI Hya system were measured with different approaches by both group-P and group-K using different spectra taken from the distinct instruments.

[1] https://mast.stsci.edu

Table 2. The results of the radial velocity analysis. The subscripts 1 and 2 refer to hotter primary and cooler secondary components, respectively. The superscript a shows the fixed parameters.

Parameter	Group-P	Group-K
T_0 (HJD)	2458491.570 ± 0.028	2452506.383 ± 0.032
P_{orb} (d)	8.289761 ± 0.000027	8.2896490^a
γ (km s^{-1})	45.90 ± 0.24	45.70 ± 0.35
K_1 (km s^{-1})	90.42 ± 0.37	89.52 ± 0.65
K_2 (km s^{-1})	83.71 ± 0.46	83.29 ± 0.63
e	0.2419 ± 0.0036	0.2432 ± 0.0050
ω (deg)	254.03 ± 1.30	250.92 ± 1.63
$\dot{\omega}$ (deg yr^{-1})	0.186 ± 0.056	
$a_1 \sin i$ ($R_\odot$)	14.380 ± 0.061	14.222 ± 0.105
$a_2 \sin i$ ($R_\odot$)	13.312 ± 0.072	13.233 ± 0.101
$a \sin i$ ($R_\odot$)	27.692 ± 0.094	27.454 ± 0.145
$M_1 \sin^3 i$ ($M_\odot$)	1.992 ± 0.023	1.950 ± 0.033
$M_2 \sin^3 i$ ($M_\odot$)	2.151 ± 0.022	2.095 ± 0.035
$q = M_2/M_1$	1.080 ± 0.007	1.075 ± 0.011

3.1 v_r measurements

Group-P calculated the v_r values from HIDES and CORALIE spectra, using the two-dimensional cross-correlation TODCOR program (Zucker & Mazeh 1994). In the analysis, a synthetic spectrum was used as a template and this spectrum was generated using an ATLAS9 model atmosphere (Kurucz 1993) having T_{eff}, metallicity [M/H], and $v \sin i$ parameters of 6800 K, 0.0, and 30 km s^{-1}, respectively. When a template with 60 km s^{-1} (the $v \sin i$ value found in further analysis) was used, the results did not improve in terms of *rms* of the orbital fit, nor did the uncertainties of orbital elements. Moreover, some points, with the smallest difference in v_r measurements, seemed to suffer from systematic effects, and had to be rejected. We therefore believe the use of 30 km s^{-1} templates was justified. The calculated v_r values for each binary component are given in Table A1.

Group-K used the RAVESPAN code (Pilecki et al. 2017) to determine the v_r values of the binary components using the broadening function (BF) formalism. In the analysis, local thermodynamic equilibrium (LTE) synthetic spectra with atmospheric parameters similar to that of group-P were used as templates (Coelho et al. 2005). The spectra of CAOS and HERMES were used in the v_r measurements. The resulting v_r measurements are given in Table A1.

3.2 v_r curve modelling

For the spectroscopic orbital fitting, group-P used all the available v_r measurements, including those made by group-K and from Popper (1988). Group-P used the V2FIT code (Konacki et al. 2010) which adjusts a double-Keplerian with a Levenberg–Marquardt algorithm. In this analysis, the amplitude of v_r curves (K), P_{orb}, the time of phase zero (T_0), mass centre's velocity (γ), eccentricity (e), and argument of the periastron (ω) were set as free parameters. Thanks to the long time span of the data (>51 yr), it was possible to detect the apsidal motion ($\dot{\omega}$) of the binary's orbit: 0.186(56) deg yr^{-1}. This is in reasonable agreement (1.75σ) with the value given by Lee et al. (2020): 0.075(31) deg yr^{-1}. The results of the analysis are given in Table 2 and the theoretical v_r curve fits to the measured v_r data are illustrated in Fig. 1.

Group-K used the RVFIT code[2] for the radial velocity analysis. The RVFIT program can analyse single and double-lined binary systems
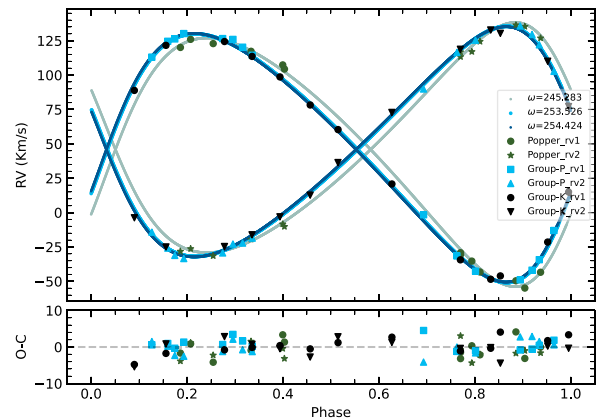
[2] http://www.cefca.es/people/riglesias/rvfit html

Figure 1. Upper panel: The model v_r fit to the combined v_r measurements from Popper (1988), Group-P (HIDES+CORALIE), and Group-K (HERMES + CAOS). Lower panel: residuals. Model made by Group-P.
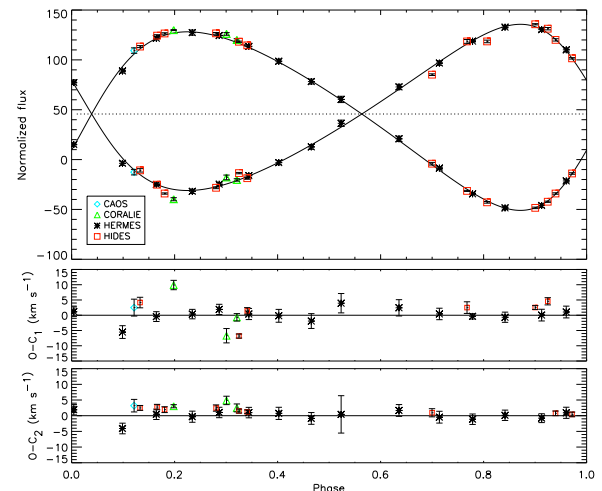

Figure 2. Upper panel: The model v_r fit to the v_r measurements of Groups-K and -P. Lower panel: residuals. Model made by Group-K.

by using the adaptive simulated annealing method (Iglesias-Marzoa, López-Morales & Jesús Arévalo Morales 2015). In the analysis, the P_{orb} taken from Kreiner (2004) was considered as a fixed parameter. Other orbital parameters such as T_0, K, γ, ω, and e were taken as free parameters during the analysis. Both groups v_r measurements were used in the analysis and as a result, the orbital parameters of the system were obtained. The resulting parameters of the current v_r analysis are given in Table 2. The consistency between the theoretical v_r curve and measurements is shown in Fig. 2.

Both groups found the resulting mass ratio ($q = M_2/M_1 = K_1/K_2$)[3] larger than 1 (1.075 ± 0.011 and 1.080 ± 0.007 for groups-K and -P, respectively). According to this q value, the v_r curve, and the results, the star (generally called secondary) covered by the hotter binary component at orbital phase 0.5 is more massive than the hotter binary component (primary). To test these findings, binary modelling is necessary. Therefore, these results will be tested in the binary modelling sections.

[3] The subscripts 1 and 2 refer to hotter primary and cooler secondary components, respectively.

4 SPECTRAL ANALYSIS

4.1 Group-K

4.1.1 Spectral disentangling

To obtain the atmospheric parameters (T_{eff}, $\log g$), $v \sin i$, and the chemical composition of each binary component of AI Hya, a detailed spectral analysis is necessary. As AI Hya is a double-lined binary system, its spectrum consists of the spectral lines of both binary components. Therefore, group-K carried out a spectral disentangling analysis to extract the individual spectra of each binary component from the composite spectra of AI Hya. In the analysis, the code FDBINARY was used (Ilijic et al. 2004). FDBINARY is capable of disentangling a composite spectrum, which includes flux contributions from two or three components, in Fourier space. Before the analysis with FDBINARY, one should know the light contributions of the binary components at the orbital phases corresponding to the times the spectra were taken. These values should be fixed during the analysis. Hence, to determine the light contributions of both binary components at the different orbital phases, we carried out a preliminary binary modelling of AI Hya by taking T_{eff} of the *TESS* Input Catalog (TIC; Stassun et al. 2019) as the T_{eff} of the hotter component. The analysis was performed utilizing the WILSON–DEVINNEY code (Wilson & Devinney 1971). As a result of this preliminary analysis, it was found that the hotter and cooler binary components contribute around 38 per cent and 62 per cent to the total, respectively. However, one should keep in mind that these light contributions change according to the orbital phases. For example, the primary eclipse is a total eclipse where the light contribution of the hotter components is negligible.

In the analysis, we used the HERMES spectra as they are well distributed over the orbital phases and have a higher resolving power. Taking into account the observation time of each HERMES spectrum, the light contributions at these times were first determined using the fluxes measured from the photometric solution and subsequently fixed during the analysis. In addition to this, we also fixed all results derived in the v_r analysis during the spectral disentangling. For the disentangling progress, we used the spectral interval of ∼4200–6400 Å by ignoring the parts polluted by telluric lines. For the analysis, this spectral window was divided into 15 spectral parts with steps of ∼100–150 Å. Each small spectral part was then analysed separately. As a result, we obtained the individual spectra of each binary component. The separated spectra derived with FDBINARY were renormalized by taking into account the light ratio of the binary components, as described by Ilijic et al. (2004).

4.1.2 Determination of the atmospheric parameters and chemical compositions

After the individual spectra of the components of AI Hya were obtained, we were able to determine the atmospheric parameters, $v \sin i$, and the chemical composition. To derive these parameters, we used the plane-parallel and line-blanketed local thermodynamic equilibrium (LTE) ATLAS9 model atmospheres (Kurucz 1993) and the SYNTHE code (Kurucz & Avrett 1981) to generate theoretical spectra. First, the hydrogen lines of the binary components were used to obtain initial T_{eff} values.

In this analysis, the H β lines of the components were compared with many theoretical H β lines which were derived for a wide range of T_{eff} (5000–9000 K) with a step size of 100 K, where $\log g$ and metallicity were fixed to 4.0 and solar, respectively. During the
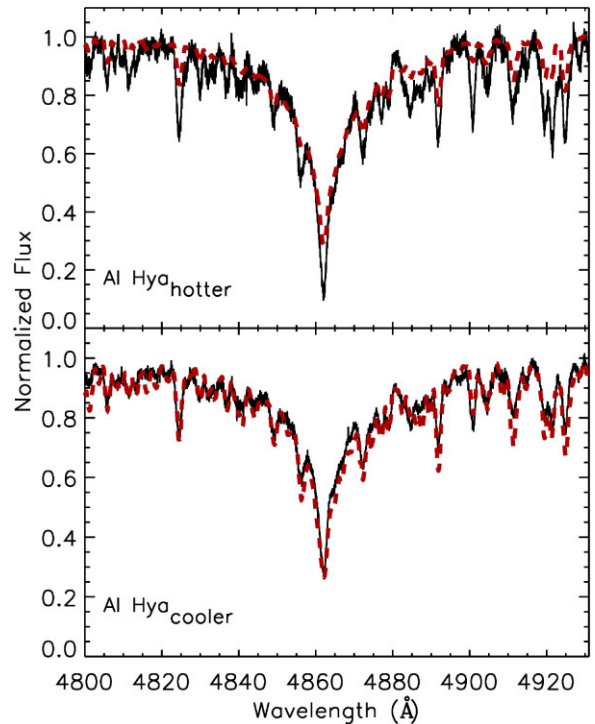

Figure 3. Theoretical hydrogen line fits (red dashed lines) to the H β lines (solid black line) of the hotter and cooler binary components (Group-K).

analysis, we took into account the minimization method described by Catanzaro, Leone & Dall (2004) and successfully applied in a series of papers (i.e. Catanzaro et al. 2019, 2022). Consequently, the T_{eff} of the hotter and cooler components were found to be 7500 ± 200 K and 7000 ± 150 K, respectively. We did not attempt to optimize $\log g$ because the hydrogen lines are not sensitive to this parameter for stars cooler than 8000 K (Smalley et al. 2002). The best theoretical H β line fits to the separated spectra of the components are shown in Fig. 3.

We also determined values for $\log g$, the microturbulent velocity ξ, and $v \sin i$ by improving the initially determined T_{eff} value using the excitation potential–abundance relationship. For the correct atmospheric parameters, different excitation potentials of the same element should give the same abundances. Therefore, by using this relation for iron (Fe), we determined the atmospheric parameters. Detailed information about this analysis method is given by Kahraman Aliçavuş et al. (2016). The results of this analysis are listed in Table 3. To determine the errors on the atmospheric parameters, we checked how their values change for differences in the excitation potential–abundance correlation of about 5 per cent.

In the next step, the chemical composition of the binary components was derived after fixing the atmospheric parameters to their final values. For the chemical abundance determination, we first identified the lines based on the Kurucz line list.[4] The spectral synthesizing method and the identified lines were used in this examination. Consequently, the chemical compositions of both binary components were obtained and the results are listed in Table 4. The consistency between the synthetic and observed spectra of both binary components is illustrated in Fig. 4. The abundance distributions relative to solar abundance (Asplund et al. 2009) are
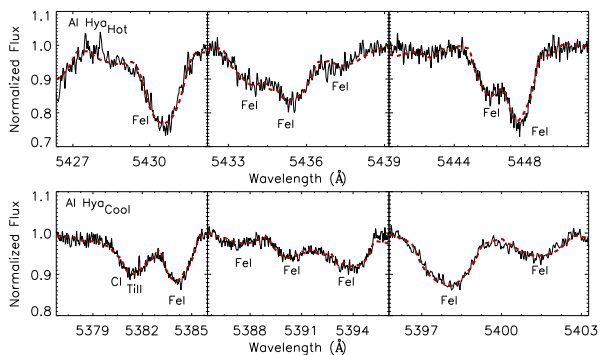
[4] http://kurucz.harvard.edu/linelists.html

Table 3. The final atmospheric parameters and $v\sin i$ value of the hot (primary) and cool binary components of AI Hya. $\log \epsilon$ (Fe) represent the relative abundance with respect to hydrogen (H = 12).

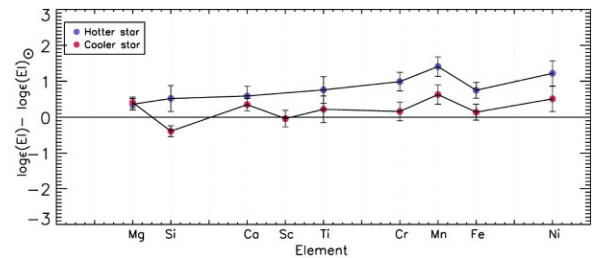|	$T_{\rm eff}$ (K)	$\log g$ (cgs)	ξ (km s^{-1})	$v\sin i$ (km s^{-1})	$\log \epsilon$ (Fe)
	Group-K				
Primary	7700 ± 100	3.8 ± 0.1	3.4 ± 0.3	57 ± 6	8.25 ± 0.54
Secondary	7200 ± 100	3.6 ± 0.2	1.9 ± 0.3	64 ± 4	7.64 ± 0.20
	Group-P (GSSP)				
	$T_{\rm eff}$ (K)	$\log g$ (cgs)	ξ (km s^{-1})	$v\sin i$ (km s^{-1})	[M/H]
Primary	7350 ± 300	3.8 (fixed)	4.83 ± 1.15	50 (fixed)	0.14 ± 0.14
Secondary	7150 ± 250	3.6 (fixed)	3.07 ± 0.52	62 (fixed)	0.06 ± 0.10
	Group-P (ISPEC)				
	$T_{\rm eff}$ (K)	$\log g$ (cgs)	ξ (km s^{-1})	$v\sin i$ (km s^{-1})	[M/H]
Primary	7300 ± 170	3.83 (fixed)	5.33 ± 0.86	50 (fixed)	0.15 (fixed)
Secondary	7260 ± 175	3.58 (fixed)	3.98 ± 0.70	62 (fixed)	0.01 (fixed)

Table 4. Abundances of individual elements of the binary components and Sun (Asplund et al. 2009).

Elements	Hotter component	Cooler component	Solar abundance
	Group-K		
$_{12}$Mg	7.96 ± 0.16	8.01 ± 0.63	7.60 ± 0.04
$_{14}$Si	8.03 ± 0.36	7.12 ± 0.51	7.51 ± 0.03
$_{20}$Ca	6.93 ± 0.27	6.69 ± 0.27	6.34 ± 0.04
$_{21}$Sc		3.11 ± 0.32	3.15 ± 0.04
$_{22}$Ti	5.71 ± 0.49	5.17 ± 0.30	4.95 ± 0.05
$_{24}$Cr	6.63 ± 0.42	5.80 ± 0.30	5.64 ± 0.04
$_{25}$Mn	6.84 ± 0.82	6.06 ± 0.45	5.43 ± 0.05
$_{26}$Fe	8.25 ± 0.23	7.64 ± 0.24	7.50 ± 0.04
$_{28}$Ni	7.44 ± 0.38	6.73 ± 0.33	6.22 ± 0.04
Elements	Hotter component	Cooler component	Solar abundance
	Group-P (ISPEC)		
$_{24}$Cr	5.95 ± 0.19	5.63 ± 0.23	5.64 ± 0.04
$_{26}$Fe	7.83 ± 0.16	7.48 ± 0.17	7.50 ± 0.04
$_{28}$Ni	6.76 ± 0.18	6.53 ± 0.22	6.22 ± 0.04

Figure 5. Abundance distribution of the components of AI Hya relative to solar values (Asplund et al. 2009) (Group-K).

4.2 Group-P

For the spectral decomposition and analysis, group-P used the HIDES data only. Spectral analysis was performed on both the observed composite spectra and the disentangled spectra of the individual components. For the spectral disentangling, we used a PYTHON wrapper[5] made for using version 3 of FDBINARY (FD3; Ilijic et al. 2004). A particular portion of the total spectra was taken to ensure good quality in terms of SNR and spectral features. The light fractions used for the disentangling procedure were obtained from the light-curve analysis as 38 per cent and 62 per cent for the primary and secondary, respectively.

4.2.1 GSSP

On the other hand, we also modelled the composite spectrum using the GSSP_COMPOSITE module of the Grid Search in Stellar Parameter (GSSP) software package (Tkachenko 2015). As its name implies, GSSP is based on a grid search in the fundamental atmospheric parameters. It uses the method of atmosphere models and spectrum synthesis, which performs a comparison of the observations with theoretical spectra from the grid. These synthetic spectra are calculated using the SYNTHV LTE-based radiative transfer code (Tsymbal 1996) and a grid of atmospheric models pre-computed using LLMODELS (Shulyak et al. 2004). Specifically, in the composite module, the user can set the radial velocity of the components as a free parameter so that all the possible combinations of the synthetic spectra of primary and secondary from the computed grid are used to build the composite theoretical spectra of the binary. This synthetic spectrum

Figure 4. Consistency between the synthetic (dashed lines) and disentangled spectra of the components of AI Hya (Group-K).

shown in Fig. 5, indicating that the hotter binary component has an overabundance compared to the Sun for some elements. The errors of the chemical compositions were determined including the uncertainties in the derived atmospheric parameters and the effects of the resolving power and the SNR of the spectra, as described by Kahraman Aliçavuş et al. (2016).

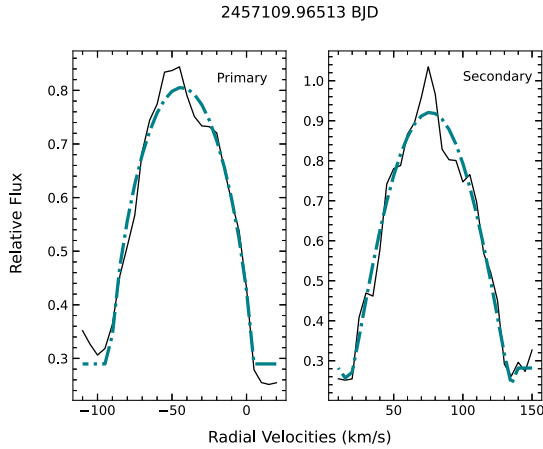[5]https://github.com/ayushmoharana/fd3_initiator

Figure 6. BFs for the primary and secondary components of AI Hydrae calculated using HIDES spectra (epoch: 2457109.96513 HJD), which provided a good SNR and velocity separation between the two components. The blue, dashed line represents best-fitting rotational function (Group-P).

is then compared against the a priori normalized observed spectrum and a χ^2 merit function is used to judge the goodness of the fit.

The BF is a representation of spectral profiles in velocity space. The BF contains signatures of the v_r shifts of different lines and also intrinsic stellar effects like rotational broadening, spots, pulsations, etc. (Rucinski 1999). We calculated the BF for one of the composite spectra of AI Hya to estimate $v \sin i$ values for the primary and secondary components, respectively. This process serves to remove the degeneracy between $v \sin i$ and other atmospheric parameters like $T_{\rm eff}$ and [M/H]. A modified version of the treatment described in Rucinski (1999) was adopted and a multi-Gaussian fit was implemented. The BF was calculated in a wavelength range of 4080–5000 Å. A synthetic solar-type spectrum with zero projected rotational velocity $v \sin i$ was used as our template. To deal with the noise in the data, a Gaussian smoother of $3 \, {\rm km \, s^{-1}}$ rolling window was applied to the BF. Two clear peaks were visible in the velocity space, as shown in Fig. 6, corresponding to the primary and secondary components. The peaks were fitted with the rotational profile,

$$G(v) = A \left[c_1 \sqrt{1 - \left(\frac{v}{v_{max}}\right)^2} + c_2 \left(1 - \left(\frac{v}{v_{max}}\right)^2\right) \right] + lv + k \quad (1)$$

where A is the area under the profile, $v_{\rm max}$ is the maximum velocity shift which occurs at the equator (Gray 2005), c_1 and c_2 are constants which are a function of limb darkening themselves, while l and k are correction factors to the BF continuum. The BF fit was calculated for the spectra with the highest SNR and good separation between the components in velocity space. The best BF fit to the line profile of the primary and secondary binary components are shown in Fig. 6. Fixing the obtained values of $v \sin i$ from this analysis and $\log g$ from the light-curve solution, the GSSP_COMPOSITE fitting routine was applied to obtain stellar temperatures $T_{\rm eff(1, 2)}$, microturbulent velocities ξ, and global metallicities [M/H].

The step size of the grid gives us a rough idea of the errors involved. However, to obtain more robust error estimates we plotted the χ^2 data for each parameter and fitted a parabola to obtain the minimum; its distance to the intercepts on the abscissa are taken as the errors. These parameters are obtained for a total of four spectra and then averaged out. The remaining spectra were not suitable for the analysis in GSSP due to lower SNR. The results of the analysis are compiled in Table 3 and a sample of the fit to one of the spectra is shown in Fig. 7.
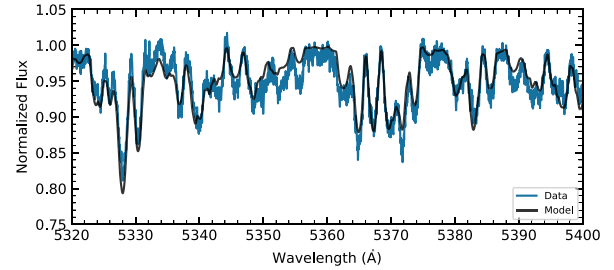
Figure 7. A snippet of the best-fitting model generated by GSSP for the given set of parameters (Group-P).

4.2.2 ISPEC

A complimentary spectroscopic analysis was performed on the disentangled spectra of the primary and secondary stars using ISPEC (Blanco-Cuaresma et al. 2014). Before the analysis, the spectra are treated for v_r offset and continuum correction. Estimates of flux errors were introduced as a sum of errors calculated from SNR, and flux-scaled residuals from the disentangled routine. For the spectroscopic analysis we fixed the $\log g$ parameter with values obtained from the light-curve solution and limb darkening parameters with values adopted from Claret & Bloemen (2011).

We fit the model using the spectral synthesis approach. This is done by implementing the use of the SPECTRUM code (Gray & Corbally 1994), a MARCS (Gustafsson et al. 2008) grid of model atmospheres, and solar abundances taken from Asplund et al. (2009). We adopt a two-step process. The initial run is aimed at estimating the global metallicity ([M/H]) by keeping it as a free parameter. The macroturbulent velocity ($v_{\rm mac}$) and alpha enhancement parameters were set to zero as $v_{\rm mac}$ has a negligible contribution for stars in the concerned temperature range and alpha enhancement, when set as a free parameter, produced implausible values. $v \sin i$ was set to the values obtained by the BF analysis. We compared the obtained value for [M/H] with results from the GSSP analysis and found it to be consistent with the errors. The average value of [M/H] was calculated and fixed for the next step where we fit for temperature $T_{\rm eff}$, microturbulent velocity ξ, and abundances of Iron (Fe), Nickel (Ni), and Chromium (Cr), as these were the prominent lines in the chosen spectral range.

The output parameters obtained from ISPEC are given in Tables 3 and 4. It is to be noted that Fe, Ni, and Cr are more abundant in the primary compared to solar values and those of the secondary star. This trend in the abundances is in agreement with the values obtained by group-K. The output parameters for the secondary star agree fairly well with those from the GSSP analysis and from the group-K. The best-fitting solution for the primary component, as in the case of GSSP analysis, also hinted towards a lower $T_{\rm eff}$ compared to the group-K solution.

5 BINARY MODELLING

5.1 Group-K

To update the fundamental stellar parameters (M, R) of AI Hya, we performed binary modelling with the help of the determined atmospheric parameters and the results of the v_r investigation.

In binary modelling, the *TESS* data were used. However, the shapes of the eclipses of AI Hya are distorted due to the pulsations. Thus we first cleaned the pulsations and only then carried out the binary modelling. Therefore, the PERIOD04 program (Lenz & Breger 2005)

Table 5. Results of the light-curve analysis and the fundamental stellar parameters. The subscripts 1, 2, and 3 represent the hotter, the cooler, and third binary components, respectively. The superscript *a* shows the fixed parameters.

Parameter	Value	Value
	Group-K	Group-P
i (deg)	89.866 ± 0.015	89.837 ± 0.136
T_1^a (K)	7700 ± 100	7330 ± 170
T_2 (K)	7180 ± 230	7210 ± 150
Ω_1	11.412 ± 0.046	–
Ω_2	8.961 ± 0.035	–
Phase shift	-0.0310 ± 0.0001	–
q	1.074^a	1.075
r_1^* (mean)	0.1001 ± 0.0036	0.1015 ± 0.0005
r_2^* (mean)	0.1412 ± 0.0026	0.1412 ± 0.0006
$l_1 / (l_1 + l_2)$	0.381 ± 0.016	0.374 ± 0.02
$l_2 / (l_1 + l_2)$	0.619 ± 0.016	0.616 ± 0.02
l_3	0.0	0.0
Derived quantities		
M_1 ($M_\odot$)	1.950 ± 0.033	1.950 ± 0.033
M_2 ($M_\odot$)	2.096 ± 0.035	2.096 ± 0.035
R_1 ($R_\odot$)	2.754 ± 0.015	2.787 ± 0.020
R_2 ($R_\odot$)	3.863 ± 0.021	3.877 ± 0.026
$\log (L_1/L_\odot)$	1.381 ± 0.034	1.311 ± 0.081
$\log (L_2/L_\odot)$	1.554 ± 0.035	1.549 ± 0.097
$\log g_1$ (cgs)	3.848 ± 0.003	3.838 ± 0.005
$\log g_2$ (cgs)	3.586 ± 0.003	3.582 ± 0.005
M_{bol1} (mag)	1.30 ± 0.08	1.474 ± 0.202
M_{bol2} (mag)	0.87 ± 0.08	0.877 ± 0.243
M_{V1} (mag)	1.25 ± 0.08	1.424 ± 0.208
M_{V2} (mag)	0.79 ± 0.08	0.822 ± 0.258
Distance (pc)	659 ± 30	642 ± 36

Figure 8. Theoretical binary modelling fit without spot assumption (solid-line) (Group-K).

and the consistency of the theoretical light curve with the observation is shown in Fig. 8.

When the results of this analysis were examined, one can notice that the more luminous star is the more massive and also the cooler component. This result is consistent with the results found in the v_r analysis by group-K.

5.2 Group-P

Aiming to determine precise physical and orbital parameters of AI Hya, we performed its modelling in version 40 of the JKTEBOP (Southworth et al. 2004). This program is written by J. Southworth and aimed at modelling light curves of detached eclipsing binaries and is based on the EBOP program (Popper & Etzel 1981). The code treats stars as spheres to calculate the eclipse shapes, and biaxial ellipsoids to calculate proximity effects. The light curves are calculated by numerical integration of concentric circles over each stellar surface. It can deal with stellar oblateness of up to 4 per cent making it a good choice for AI Hya. The photometric data remain the same as used by Group-K.

The parameters set as free are P_{orb}, time of minima of the primary eclipse T_o, inclination i, eccentricity e, argument of periastron ω, surface brightness ratio J (secondary/primary), ratio of radii ($\frac{r_A}{r_B}$), and the sum of radii ($r_A + r_B$). These radii are relative to the semimajor axis. For the limb darkening coefficients, we use a logarithmic law and set their initial values according to Claret (2017). The coefficients were fixed for the initial fit and were perturbed at the error estimation step.

The code gives an option to include multiple sine and polynomial functions during the light-curve modelling to account for periodic and long-term trends. We use this functionality to our advantage to pseudo-model the observed pulsations so that their effect on the binary model is minimal, giving us an improved precision. We analyse the out-of-eclipse portions of the light curve using PYRIOD,[7] and use the frequencies to initialize the sinusoids in the JKTEBOP input files. This is done in an iterative way where we add one sine with a constant period and fit for its epoch and amplitude. The frequency is kept if the model is improved significantly; otherwise the next most

was used to detect the variations caused by oscillations. The derived pulsation frequencies[6] were cleaned from the light curve and the residuals were used in the binary modelling.

In this analysis, we used the WILSON–DEVINNEY code (Wilson & Devinney 1971) combined with Monte Carlo simulations (Zola et al. 2004, 2010). The pulsation removed data were binned to around 4000 points to be used in the binary modelling code. AI Hya is classified as a detached binary system in the literature (Lee et al. 2020). According to their results (e.g. for Ω, q, a), both components do not seem to fill their Roche lobe, hence the system is defined as a detached binary. Also, the morphology of the light curve, i.e. very small ellipsoidal variations and eclipses spanning a small fraction of the orbital period, confirm this classification. Therefore, a detached binary configuration was considered our analysis. In the modelling, we took some parameters fixed, such as the T_{eff} of the hotter component, P_{orb}, q taken from our results and bolometric albedos (Ruciński 1969), bolometric gravity-darkening coefficient (von Zeipel 1924), and the logarithmic limb darkening coefficient (van Hamme 1993) taken the same as given (Kahraman Aliçavuş & Aliçavuş 2019). The orbital inclination (i), T_{eff} of the cooler component, phase shift (ϕ), e, a, ω, and dimensionless potential (Ω) of the components were set free.

As a result of this analysis, the fundamental parameters of both components of AI Hya were calculated. Additionally, the bolometric (M_{bol}) and absolute (M_V) magnitudes were estimated. The JKTABSDIM code (Southworth, Maxted & Smalley 2004) and the bolometric correction (Eker et al. 2020) are used in the calculations of these parameters. The outcome of the binary modelling is given in Table 5
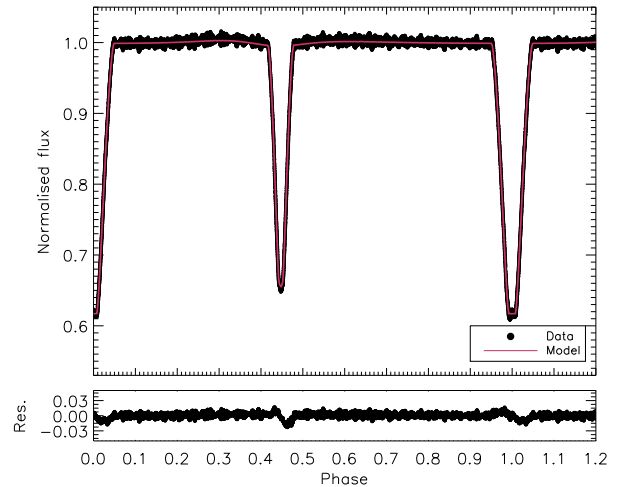
---

[6]The frequencies given in Section 6.

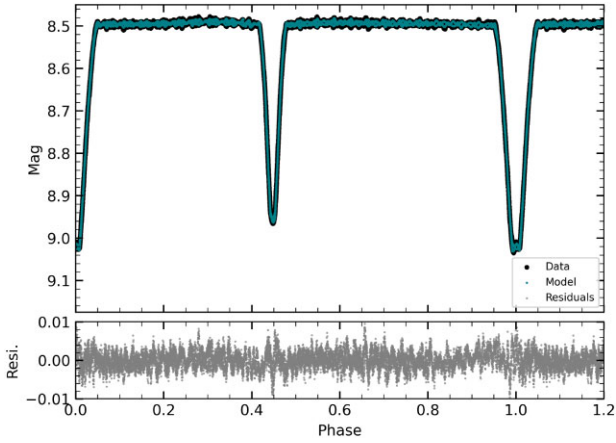[7]https://github.com/keatonb/Pyriod

Figure 9. JKTEBOP model with 9 sines used to model the pulsations (Group-P).
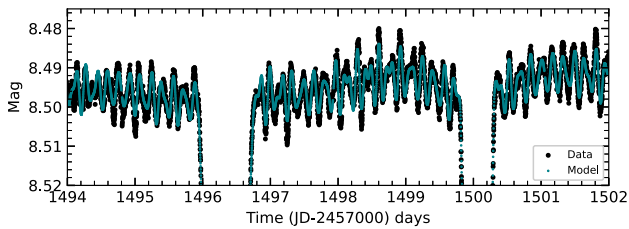

Figure 10. Zoomed-in view of the model over an orbit (Group-P).

prominent frequency is taken. In this analysis, we used a total of 9 sines, which is the limit for JKTEBOP. The number of independent frequencies of AI Hya is higher than this maximum limit, hence we are left with some residual pulsation signals as seen in Figs 9 and 10.

Once the sines are fixed to the best-fitting values of epoch, period, and amplitudes, we make the Monte Carlo runs for error estimation. The results of this analysis are mentioned in Table 5, in comparison to the values obtained by group-K. Similarly to the other group, we used the results of v_r, and JKTEBOP solutions to calculate a set of absolute parameters, including masses, radii, luminosities, and distance. The effective temperatures mentioned in the table are an average over the sum of T_{eff} obtained from GSSP and ISPEC analysis.

6 FREQUENCY ANALYSIS OF THE PULSATIONS

AI Hya was observed by *TESS* during observation sector 7 in 2019 January/February. We used the Simple Aperture Photometry data from the 2-min cadence light curves available at the Mikulski Archive for Space Telescopes[8] (MAST). This time series spans 24.45 d and contains 16 362 measurements. To determine the pulsation frequencies, we used only the data that were taken out of eclipse, which reduced the data set to 14 019 measurements (time span 24.07 d).

This time series was analysed using the PERIOD04 software (Lenz & Breger 2005) by group-K. This package applies single-frequency power spectrum analysis and simultaneous multifrequency sine-wave fitting. These sine-wave fits are subtracted from the data
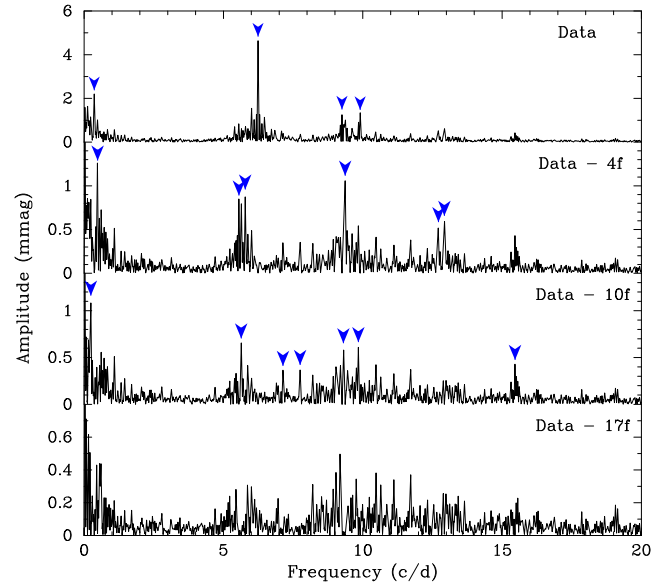
[8] https://mast.stsci.edu/portal/Mashup/Clients/Mast/Portal.html

Figure 11. The Fourier Transform of the out-of-eclipse *TESS* light curve of AI Hya (top) and subsequent prewhitening steps. The blue arrows denote the signals detected. Outside of the frequency range shown no significant signal is present.

and the residuals examined for the presence of further periodicities. The application of this procedure to AI Hya is illustrated in Fig. 11.

During such a process, it is important to decide where to stop. Often this is facilitated via the application of SNR criteria. In this work, we have adopted the strategy proposed by Breger et al. (1993) which is to compute the ratio of the signal amplitude relative to the local noise level to determine whether the frequency under consideration represents a significant detection. Whereas Breger et al. (1993) propose SNR > 4 for a detection, recent findings for space-based data (e.g. Baran & Koen 2021) suggest that a more conservative limit must be chosen. Given the restricted frequency range in which we search for periodicities, our requirement was SNR > 4.5. Furthermore, in unresolved frequency spectra, the periodic content present in the time series can easily be overinterpreted (Balona 2014) which suggests caution regarding the present data set. Consequently, we stopped the frequency search after the detection of 17 signals (lowest panel of Fig. 11). More periodicities are certainly present, but these need to await a longer data set for reliable detection. We list the frequency solution so derived in Table 6.

This table also contains three harmonics of the orbital period. These are not pulsation frequencies, but a consequence of residual binary-induced variability (see Section 5 for a discussion). The pulsation frequencies themselves were found in an interval between 5.5 and 13.0 d^{-1}, with one possible combination frequency. It is however not clear whether this is a real combination or just a numerical coincidence keeping in mind the short data set, hence poor frequency resolution. Our frequency solution is similar to that reported by Lee et al. (2020) apart from their identification of possible combination frequencies that are partly implausible.

To use the pulsations to learn more about the individual components by applying asteroseismic methods, it is essential to know from which star the pulsations originate. A quick look at the *TESS* light curve reveals that pulsations are clearly visible during the total part of the primary eclipse, meaning that the secondary is the source of the highest amplitude oscillations. However, both components of AI Hya are located within the pulsational instability strip of the

Table 6. A least-squares fit of the pulsation frequencies of AI Hya. Formal error estimates for the independent frequencies and phases (Montgomery & O'Donoghue 1999) are given in braces in units of the last digits after the comma.

	Frequency d^{-1}	Amplitude mmag ±0.02	SNR
ν_1	6.2412(1)	4.75	54.2
ν_2	9.2654(4)	1.18	9.7
ν_3	9.9065(4)	1.20	9.4
ν_4	12.715(1)	0.48	4.5
ν_5	12.928(1)	0.54	5.4
ν_6	9.3689(4)	1.42	11.5
$3\nu_{orb}$	0.3619	1.76	7.5
$4\nu_{orb}$	0.4825	1.32	5.9
ν_7	5.5599(7)	0.78	8.3
ν_8	5.7804(1)	0.69	7.5
$2\nu_{orb}$	0.2413	1.75	7.3
ν_9	5.6375(7)	0.73	7.7
ν_{10}	7.136(1)	0.37	6.0
ν_{11}	7.751(1)	0.39	5.2
ν_{12}	9.3051(6)	0.82	6.7
ν_{13}	9.8432(8)	0.69	5.3
$\nu_3 + \nu_7$	15.464(1)	0.43	5.6

Table 7. Results obtained from the best-fitting evolutionary models.

| Parameter	Group-K	Group-P
$P_{initial}$ (d)	8.34 (1)	8.34 (1)
$e_{initial}$	0.242 (2)	0.243 (2)
Z_1	0.013 (2)	0.016 (2)
Z_2	0.018 (2)	0.018 (2)
Age (Myr)	850 (20)	860 (20)

Figure 12. The positions of the binary components in the H–R diagram according the results of both group-K (g-K) and group-P (g-P). The instability strip (IS) borders of the δ Scuti stars were taken from Murphy et al. (2019).

δ Scuti stars (Murphy et al. 2019, see fig. 12), thus the primary may pulsate as well. δ Scuti stars generally pulsate in pressure and mixed modes of low radial order (e.g. Breger 2000). Using the stellar parameters from Table 5, we can compute the expected frequency of the radial fundamental mode of both pulsators from the pulsation constant $Q = P\sqrt{\rho/\rho_\odot} = PM^{1/2}R^{-3/2}$, assuming Q to be 0.033 d for this mode (Fitch 1981). We thus expect the radial fundamental mode frequency of the primary component to be around 9.3 d^{-1}, and around 5.8 d^{-1} for the secondary component, respectively. In Table 6, oscillation frequencies around both these values are seen, which allows no more than the educated guess that the pulsations below ~ 8 d^{-1} would arise from the secondary component, whereas the higher frequency modes could originate from either star.

A determination of the origin of the pulsations from the orbital light time effect is unfortunately out of reach. The expected light time effect would be about 30 s (cf. Table 2). An attempt to measure the effect for the strongest pulsation frequency yielded 35 ± 111 s, a null result. To conclude, because it is impossible to say with confidence which pulsation frequencies arise from which component of AI Hya, an asteroseismic analysis cannot be carried out.

7 EVOLUTIONARY MODELS

The evolutionary status of the binary components was examined by utilizing the Modules for Experiments in Stellar Astrophysics (MESA) evolution code (Paxton et al. 2011, 2013) which includes a binary module (Paxton et al. 2015) to examine the binary orbital evolution and to determine the initial parameters of binary systems. In this examination, various evolutionary models were generated considering different metallicity (Z). In the models, MESA equation-of-state (EOS) were used. The EOS tables are based on the OPAL EOS tables (Rogers & Nayfonov 2002). The OPAL opacity tables and the default solar mixtures were adopted as Z initial fraction from Asplund et al. (2009). Helium mass fraction were taken $Y = 0.28$, for $Z = 0.02$. Convective core overshoot was described by the exponentially decaying prescription of Herwig (2000) and overshooting parameter adopted 0.20 for both components (Claret &
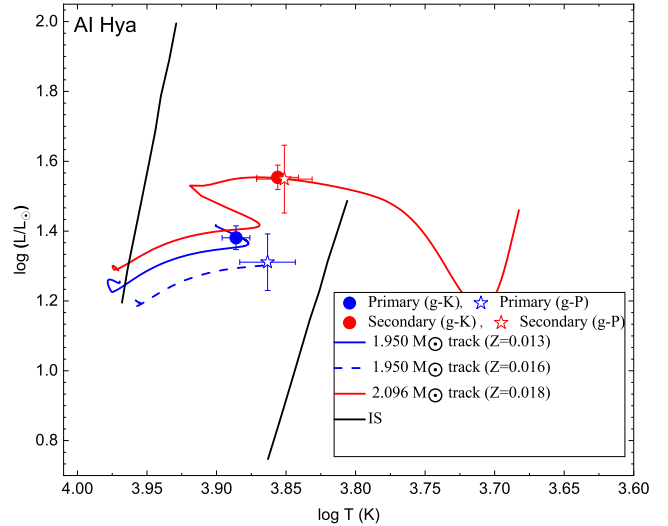
Torres 2016 find 0.208 for both components). A mixing length α_{MLT} value of 1.8 was used as the theoretical δ Scuti instability strip (Dupret et al. 2004, 2005) was obtained with this α_{MLT} value.

Taking into account the calculated parameters in the binary modelling for both groups, the evolutionary status of the binary components was investigated. As a result, we found that the secondary (more luminous) binary component can be represented with the same evolutionary tracks according to both groups' results. However, the less luminous primary component's position was determined with different Z parameters as the parameters of this star were found to be slightly different in the study of the two groups. According to the evolutionary models, the Z parameters of both binary components were found similar to solar (Asplund et al. 2009) within the errors which differs from the results of the groups as we determined that the less luminous component's atmosphere is somewhat enhanced in metals. The results of this analysis are given in Table 7 and a H–R diagram is shown in Fig. 12. The observational borders of the δ Scuti instability strip were taken from Murphy et al. (2019). As can be seen from the H–R diagram, both binary components are placed inside the δ Scuti instability strip.

8 DISCUSSION AND CONCLUSIONS

In this analysis, we present the results of the detailed analysis of AI Hya carried out by two independent groups. The system was observed with different high-resolution spectrographs ($R \gtrsim 38\,000$). The radial velocity variations of AI Hya were modelled using the v_r measurements of both groups and the orbital parameters such as T_0, P_{orb}, e, and q were updated. The resulting parameters of the

analysis of both groups are consistent with each other within the errors and they slightly differ from the results of Popper (1988). Especially the *e* value shows a discrepancy. Popper (1988) found *e* to be 0.2301 ± 0.0015 while in our study it was determined as 0.2419 ± 0.0036 and 0.2432 ± 0.0050 by group-P and -K, respectively.

Since our high-resolution spectra are spread over all orbital phases, we were able to derive the atmospheric parameters of both binary components by modelling either the composite spectra or the spectra of the individual components after applying spectral disentangling. To derive the atmospheric parameters, $v \sin i$ and the chemical composition of the binary components, group-K analysed disentangled spectra of the components, while group-P performed their analysis using both the composite and disentangled spectra. As a result, group-K found that the more luminous star is cooler than the less luminous component. They found the $T_{\rm eff}$ values from the H β line fit and Fe lines to be 7500 ± 200 K and 7700 ± 100 K for the primary and 7000 ± 150 K and 7200 ± 100 K for the secondary component, respectively. Group-P used two different codes in their analysis. With the GSSP code analysis they found a similar result with group-K even though the resulting $T_{\rm eff}$ values differ from each other, they determined that the more luminous star is cooler (7150 ± 250 K) and less luminous one is hotter (7350 ± 300 K). In the ISPEC analysis of group-P, $T_{\rm eff}$ values of both components were found similar to the results of the GSSP analysis within error bars. The primary's temperature is the most significant discrepancy between the values derived by the two groups. The exact reason for this temperature inconsistency is not fully understood, although it is still only at a level of $\sim 1.1\sigma$.

In the chemical abundance analysis, both groups found the less luminous but hotter binary component to show overabundance while the other component has chemical abundance similar to solar. Both groups determined the abundances of some individual elements such as iron (Fe). They derived Fe abundances as 8.25 ± 0.23 (group-K) and 7.83 ± 0.16 (group-P). These values are consistent with each other within their 1σ errors, and both demonstrate that the hotter component has a slightly metal-rich chemical abundance compared to solar values (see Table 4). This comes somewhat to a surprise, as this binary system should have been formed in the same interstellar environment and hence its components should have the same chemical composition. The difference could be due to the consequences of the evolution of the system. If AI Hya had a very eccentric orbit when the system was formed, there could be some material flows from one component to another that could have changed the diffusion in one component. Another explanation was given by Yushchenko et al. (2015) and they pointed out that possible gas and dust accretion from the circumstellar envelope could alter the atmospheric composition of one component.

After the determination of the atmospheric parameters, they were used as input in the binary modelling. Overall, even though both working groups used different approaches to estimate the parameters of the binary component of AI Hya, the values determined by both groups are found to be consistent with each other within the error bars. The two groups obtained very similar *M* and *R* values with a ≤ 1.7 per cent and ~ 0.5 per cent accuracy, respectively. When we compare these values with the ones found by Lee et al. (2020), we notice that there are slight differences, especially in the *R* parameters, and there is significant diversity in the calculated distance. These differences could be caused by the different assumptions of the atmospheric parameters.

The evolutionary status of the system was examined and it was found that both binary components are inside the δ Scuti instability strip. The age of the system is determined as well. According to the determined ages, we could say that AI Hya is in an important evolutionary phase in terms of binary evolution. The rapidly evolving massive component will begin the mass transfer process to the less massive one approximately 20 Myr from now. This situation could cause significant variations in the oscillation properties. Increasing the number of such bodies is important in terms of examining the pulsating structures before the mass transfer processes.

The pulsation properties of AI Hya were examined using the *TESS* data. However, the system has only one sector of SC data, which offers us a poor frequency resolution. In the analysis, pulsation frequencies were found between 5.5 and 13 d^{-1}. As both binary components are placed in the δ Scuti instability strip, we were unable to say whether one or both pulsate. Apart from that, we could not find pulsations related to the orbital frequency.

As a result of this study, we thoroughly examined a detached binary system showing oscillations. This kind of objects is particularly important to examine the instability strip of δ Scuti stars since they allow us to determine fundamental astrophysical, atmospheric parameters, and the chemical abundances of individual binary components. Hence an increasing number of analyses of such systems is expected to be essential to deeply understand the nature of pulsations.

DATA AVAILABILITY

The data underlying this work will be shared at reasonable request to the corresponding author.

REFERENCES

Aerts C., Christensen-Dalsgaard J., Kurtz D. W., 2010, Asteroseismology, Springer Science+Business Media B.V
Antoci V. et al., 2014, ApJ, 796, 118
Asplund M., Grevesse N., Sauval A. J., Scott P., 2009, ARA&A, 47, 481
Balona L. A., 2014, MNRAS, 439, 3453

Baran A. S., Koen C., 2021, Acta Astron., 71, 113
Blanco-Cuaresma S., Soubiran C., Heiter U., Jofré P., 2014, A&A, 569, A111
Borucki W. J. et al., 2010, Science, 327, 977
Bowman D. M., Kurtz D. W., 2018, MNRAS, 476, 3169
Breger M., 2000, in Breger M., Montgomery M. H., eds, ASP Conf. Ser. Vol. 210, Delta Scuti and Related Stars. Astron. Soc. Pac., San Francisco, p. 3
Breger M. et al., 1993, A&A, 271, 482
Catanzaro G., Leone F., Dall T. H., 2004, A&A, 425, 641
Catanzaro G., Busà I., Gangi M., Giarrusso M., Leone F., Munari M., 2019, MNRAS, 484, 2530
Catanzaro G., Colombo C., Ferrara C., Giarrusso M., 2022, MNRAS, 515, 4350
Claret A., 2017, A&A, 600, A30
Claret A., Bloemen S., 2011, A&A, 529, A75
Claret A., Torres G., 2016, A&A, 592, A15
Coelho P., Barbuy B., Meléndez J., Schiavon R. P., Castilho B. V., 2005, A&A, 443, 735
Dupret M.-A., Grigahcène A., Garrido R., Gabriel M., Scuflaire R., 2004, A&A, 414, L17
Dupret M.-A., Grigahcène A., Garrido R., Gabriel M., Scuflaire R., 2005, A&A, 435, 927
Eker Z. et al., 2020, MNRAS, 496, 3887
Fitch W. S., 1981, ApJ, 249, 218
Gaulme P., Guzik J. A., 2019, A&A, 630, A106
Gray D. F., 2005 The Observation and Analysis of Stellar Photospheres, Cambridge University Press
Gray R. O., Corbally C. J., 1994, AJ, 107, 742
Gustafsson B., Edvardsson B., Eriksson K., Jørgensen U. G., Nordlund Å., Plez B., 2008, A&A, 486, 951
Handler G. et al., 2020, Nat. Astron., 4, 684
Herwig F., 2000, A&A, 360, 952
Iglesias-Marzoa R., López-Morales M., Jesús Arévalo Morales M., 2015, PASP, 127, 567
Ilijic S., Hensberge H., Pavlovski K., Freyhammer L. M., 2004, in Hilditch R. W., Hensberge H., Pavlovski K., eds, ASP Conf. Ser. Vol. 318, Spectroscopically and Spatially Resolving the Components of the Close Binary Stars. Astron. Soc. Pac., San Francisco, p. 111
Jayasinghe T. et al., 2018, MNRAS, 477, 3145
Kahraman Aliçavuş F., Aliçavuş F., 2019, MNRAS, 488, 5279
Kahraman Aliçavuş F. et al., 2016, MNRAS, 458, 2307
Kahraman Aliçavuş F., Soydugan E., Smalley B., Kubát J., 2017, MNRAS, 470, 915
Kahraman Aliçavuş F., Gümüş D., Kırmızıtaş Ö., Ekinci Ö., Çavuş S., Kaya Y. T., Aliçavuş F., 2022, Res. Astron. Astrophys., 22, 085003
Kambe E. et al., 2013, PASJ, 65, 15, §
Konacki M., Muterspaugh M. W., Kulkarni S. R., Hełminiak K. G., 2010, ApJ, 719, 1293
Kreiner J. M., 2004, Acta Astron., 54, 207
Kurtz D. W. et al., 2020, MNRAS, 494, 5118
Kurucz R., 1993, Kurucz CD-ROM, ATLAS9 Stellar Atmosphere Programs and 2 km/s grid, Cambridge
Kurucz R. L., Avrett E. H., 1981, SAO Special Report #391
Lampens P., 2021, Galaxies, 9, 28
Lee J. W., Hong K., Kristiansen M. H., 2020, PASJ, 72, 37
Lenz P., Breger M., 2005, Commun. Asteroseismol., 146, 53
Leone F. et al., 2016, AJ, 151, 116
Liakos A., Niarchos P., 2017, MNRAS, 465, 1181
Montgomery M. H., O'Donoghue D., 1999, Delta Scuti Star Newsletter, 13, 28
Murphy S., Hey D., Van Reeth T., Bedding T., 2019, MNRAS, 485, 2380
Paxton B., Bildsten L., Dotter A., Herwig F., Lesaffre P., Timmes F., 2011, ApJS, 192, 3
Paxton B. et al., 2013, ApJS, 208, 4
Paxton B. et al., 2015, ApJS, 220, 15
Pepe F., Bouchy F., Mayor M., Udry S., 2018, Handbook of Exoplanets
Pilecki B. et al., 2017, ApJ, 842, 110
Pojmański G., 2002, Acta Astron., 52, 397
Popper D. M., 1988, AJ, 95, 190
Popper D. M., Etzel P. B., 1981, AJ, 86, 102
Raskin G. et al., 2011, A&A, 526, A69
Ricker G. R. et al., 2014, in Oschmann Jr. J. M., Clampin M., Fazio G. G., MacEwen H. A., eds, Proc. SPIE Conf. Ser. Vol. 9143, Space Telescopes and Instrumentation 2014: Optical, Infrared, and Millimeter Wave. SPIE, Bellingham, p. 914320
Rogers F. J., Nayfonov A., 2002, ApJ, 576, 1064
Ruciński S. M., 1969, Acta Astron., 19, 245
Rucinski S., 1999a, in Hearnshaw J. B., Scarfe C. D., eds, ASP Conf. Ser. Vol. 185, IAU Colloq. 170: Precise Stellar Radial Velocities. Astron. Soc. Pac., San Francisco, p. 82
Rucinski S., 1999b, Turk. J. Phys., 23, 271
Shulyak D., Tsymbal V., Ryabchikova T., Stütz C., Weiss W. W., 2004, A&A, 428, 993
Smalley B., Gardiner R. B., Kupka F., Bessell M. S., 2002, A&A, 395, 601
Southworth J., 2013, A&A, 557, A119
Southworth J., 2021, Universe, 7, 369
Southworth J., Zucker S., Maxted P. F. L., Smalley B., 2004, MNRAS, 355, 986
Stancliffe R. J., Fossati L., Passy J.-C., Schneider F. R. N., 2015, A&A, 575, A117
Stassun K. G. et al., 2019, AJ, 158, 138
Tkachenko A., 2015, A&A, 581, A129
Torres G., Andersen J., Giménez A., 2010, A&AR, 18, 67
Tsymbal V., 1996, in Adelman S. J., Kupka F., Weiss W. W., eds, ASP Conf. Ser. Vol. 108, Model Atmospheres and Spectrum Synthesis. Astron. Soc. Pac., San Francisco, p. 198
Uytterhoeven K. et al., 2011, A&A, 534, A125
van Hamme W., 1993, AJ, 106, 2096
von Zeipel H., 1924, MNRAS, 84, 665
Wilson R. E., Devinney E. J., 1971, ApJ, 166, 605
Yushchenko A. V. et al., 2015, AJ, 149, 59
Zola S. et al., 2004, Acta Astron., 54, 299
Zola S., Gazeas K., Kreiner J. M., Ogloza W., Siwak M., Koziel-Wierzbowska D., Winiarski M., 2010, MNRAS, 408, 464
Zucker S., Mazeh T., 1994, ApJ, 420, 806

APPENDIX

Table A1. The v_r measurements. The subscripts '1' and '2' represent the more and the less luminous components, respectively.

HJD + 2450000	$v_{r,1}$ (km s^{-1})	$v_{r,2}$ (km s^{-1})	Instrument
9263.45270	-12.6 ± 2.8	109.3 ± 2.7	CAOS
9161.65803	132.8 ± 1.8	-48.3 ± 1.7	HERMES
9162.64306	109.8 ± 2.0	-21.7 ± 1.5	HERMES
9230.65226	121.5 ± 1.6	-24.7 ± 1.8	HERMES
9231.66393	124.1 ± 1.7	-24.9 ± 1.7	HERMES
9233.62648	59.8 ± 5.7	36.1 ± 3.4	HERMES
9234.55784	20.6 ± 2.1	72.1 ± 2.5	HERMES
9237.61273	15.0 ± 1.6	77.3 ± 1.5	HERMES
9235.43315	-46.3 ± 1.5	130.3 ± 1.8	HERMES
9257.49195	98.8 ± 1.8	-2.9 ± 2.0	HERMES
9260.61123	-33.9 ± 1.7	117.9 ± 1.9	HERMES
9276.55613	96.6 ± 2.0	-8.4 ± 1.2	HERMES
9296.42427	88.7 ± 1.7	-3.8 ± 2.0	HERMES
9297.44747	126.7 ± 1.8	-37.4 ± 2.2	HERMES
9298.45846	113.5 ± 1.7	-16.0 ± 1.8	HERMES
9299.46357	78.1 ± 2.1	12.5 ± 2.3	HERMES
7075.62231	-39.7 ± 1.5	129.9 ± 0.5	CORALIE
7076.63954	-20.4 ± 1.2	120.0 ± 1.3	CORALIE
7109.63123	-17.9 ± 2.4	126.0 ± 1.3	CORALIE
7022.31643	118.5 ± 1.9	-31.4 ± 0.5	HIDES
7060.09414	-13.6 ± 0.7	118.2 ± 0.6	HIDES
7109.96513	-18.6 ± 1.1	114.6 ± 0.6	HIDES
7114.92732	120.1 ± 1.2	-34.0 ± 0.7	HIDES
7146.98403	118.5 ± 1.3	-42.9 ± 0.8	HIDES
7147.96084	131.3 ± 1.2	-42.3 ± 0.6	HIDES
7363.28986	135.7 ± 0.6	-48.4 ± 0.7	HIDES
7755.22744	-34.0 ± 0.7	126.5 ± 0.7	HIDES
7813.13416	-25.2 ± 0.8	124.3 ± 0.9	HIDES
7814.08321	-28.3 ± 0.9	126.6 ± 0.9	HIDES
7846.01822	-10.8 ± 1.7	113.4 ± 1.0	HIDES
8035.34461	101.6 ± 0.7	-13.9 ± 0.8	HIDES
8066.24908	85.2 ± 0.8	-4.1 ± 1.3	HIDES

This paper has been typeset from a TEX/LATEX file prepared by the author.